


Article

# A Flux-Controllable NI HTS Flux-Switching Machine for Electric Vehicle Applications

Young Jin Hwang \*, Jae Young Jang and SangGap LeeCenter for Scientific Instrumentation, Korea Basic Science Institute, Daejeon 34133, Korea;  
gangaji2080@kbsi.re.kr (J.Y.J.); sgl757@kbsi.re.kr (S.L.)

\* Correspondence: yjhwang@kbsi.re.kr; Tel.: +82-43-240-5358

Received: 13 February 2020; Accepted: 24 February 2020; Published: 25 February 2020



**Abstract:** This paper deals with a flux-controllable NI HTS flux-switching machine (FSM) for electric vehicle (EV) applications. In a variable-speed rotating machine for EVs, such as electric buses, electric aircraft and electric ships, an electric motor capable of regulating the flux offers the advantage of constant output operation. In general, conventional HTS rotating machines have excellent flux-regulation performance, because they excite an HTS field coil. However, it is difficult to ensure any flux-regulation capabilities in HTS rotating machines using HTS field coils that apply the no-insulation (NI) winding technique, due to the inherent charge and discharge delays in these machines. Nevertheless, the NI winding technique is being actively researched as a key technology for the successful development of HTS rotating machines, because it can dramatically improve the operational stability of HTS field coils. Therefore, research to implement an HTS rotating machine with flux-regulation capabilities, while improving the operating stability of the HTS field coil using the NI winding technique, is required for EV applications. In this paper, we propose an HTS rotating machine with a flux switching structure, a type of topology of a rotating machine that is being actively studied for application to the electric motors used in EVs. The proposed HTS flux-switching machine (FSM) uses NI field coils, but additional field windings are applied for flux regulation, which enables flux control. In this study, an NI HTS field coil was also fabricated and tested because the characteristic resistance value should be used for the design and characteristic analyses of machines which utilize an NI coil. The simulation model used to analyze the flux-regulation performance capabilities of the NI HTS FSM were devised based on the characteristic resistance values obtained from a charging test of the fabricated NI HTS field coil. This study can provide a good reference for further research, including work on the manufacturing of a prototype NI HTS FSM for EV applications, and it can be used as a reference for the development of other HTS rotating machines, such as those used in large-scale wind power generation, where flux-regulation capabilities are required.

**Keywords:** electric vehicle; flux regulation; flux-switching machine; HTS; no-insulation

## 1. Introduction

Currently, electric vehicles (EVs) are regarded as good candidates for decreasing environmental pollution by reducing the use of fossil fuels [1–7]. Accordingly, there has been rapid progress in the creation of electric vehicles. An EV, also known as an electric vehicle, is a type of transportation which uses electric motors for propulsion in place of a conventional propulsion system, such as an internal combustion engine (ICE). EVs can include electric cars, electric buses, electric trucks, electric trains, electric aircraft, electric scooters and even electric ships. Motion in EVs can be provided by wheels or propellers driven by traction motors, or in the case of railway vehicles, by linear motors.

Two types of electric motors are commonly used for vehicle applications: The induction motor (IM), and the permanent magnet synchronous motor (PMSM), and it is generally known that IMs have

lower rated torque and efficiency levels compared to PMSMs. In general, PMSMs are more efficient, and for this reason electric vehicles commonly use these types of electric motors. However, because a PMSM uses constant magnetic flux generated by PMs, the flux can only be regulated by means of an armature reaction flux control by a converter. This decreases the machine efficiency, because it significantly increases the winding losses. While PMSMs have employed innovative technologies, it is not easy to increase the electric motor output power any further.

As an advanced technology for electric motors, researchers have made progress on the development of high-temperature superconducting rotating machines. Because superconducting wires can handle high-density current flows well, compared to copper wire, it is possible to manufacture a coil capable of generating a very high magnetic field, even with a low number of windings using superconducting wires. Therefore, by applying superconducting coils to electrical machines such as a motor and generator, it is possible to develop electrical machines with high efficiency and high output power levels. Accordingly, many researchers have attempted to apply superconducting motors to EVs, and the applicability of superconducting motors has been largely verified [8–15]. However, for the practical application of superconducting motors to EVs, the operating stability and reliability must be improved. Superconductors can exhibit superconductivity only under critical environmental conditions, such as those with a critical current, critical temperature and critical magnetic field, and superconductivity is lost when this condition deviates for any reason. If this phenomenon, called quenching, occurs, superconductors gain electrical resistance, which can lead to Joule heating and damage. In particular, such damage can be a serious problem in high-temperature superconducting (HTS) wires, given their relatively slow normal zone propagation velocities. Therefore, in order to apply superconducting coils wound with HTS wiring to electrical machines, it is very important to protect the HTS coils from the quenching phenomenon. The approach known as the no-insulation (NI) winding technique is a viable quench-protection method for HTS coils [16–25]. The NI winding technique involves the fabrication of coils without insulation materials between the turns. Figure 1 shows the quench-protection mechanism of the NI winding technique. In this figure,  $I_{op}$  is the operating current flowing through the coil. For an HTS coil with turn-to-turn insulation, even if a hot spot occurs due to a partial quench, the current flows continuously through the hot spot, meaning that Joule heat is continuously generated. On the other hand, an NI coil without turn-to-turn insulation has a self-protection mechanism, in that it bypasses the current to the adjacent turns automatically when the HTS coil is partially quenched. Given that the electrical resistance of the superconducting layer under the normal operation condition is nearly zero, the current flows only to the superconducting layer. However, when a hot spot caused by local quenching occurs, electrical resistance occurs at the local portion. Therefore, the current flows through the stabilizer layer constituting the superconducting wire, and it is thus bypassed. As a result, NI coils can be protected from quenching without complicated quench detection schemes and/or protection devices, simplifying these HTS coil systems [16–25]. However, the NI HTS coil is associated with an intrinsic charging/discharging delay phenomenon. The charging/discharging delay phenomenon increases as the coil inductance increases, and the contact resistance between winding turns decreases. Figure 2 shows a circuit model of the NI HTS coil. In this figure, the portion indicated by the light blue background represents the simplified equivalent circuit model of the NI HTS coil. As indicated by this circuit model, when the current is charged or discharged, the current in the NI HTS coil is divided into a spiral direction (winding direction) and a radial direction (contact direction between winding turns). The division ratio of the current is determined by the ratio of the azimuthal impedance value, which is in turn determined by the coil inductance and the current charge/discharge rate to the radial impedance value due to the characteristic resistance. The magnetic field generated by the coil stems from the current flowing in the spiral direction. Therefore, if the coil inductance is large, the current flowing through the contact becomes large, such that the delay phenomenon during the charge and discharge of the magnetic field becomes very large. Therefore, in order to develop a robust electric motor using an NI coil, the effects by these charge and discharge delays should be considered.

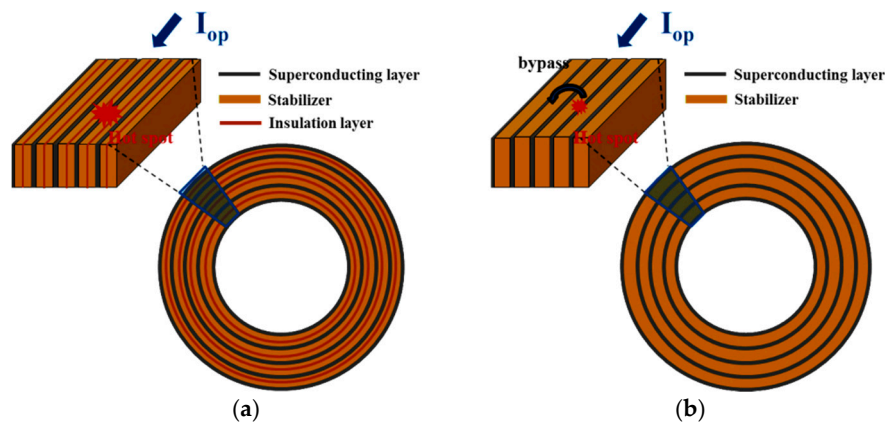


**Figure 1.** Illustration of the self-protection mechanism of the no-insulation (NI) superconducting coil in a comparison: (a) high-temperature superconducting (HTS) coil using the turn-to-turn winding technique, and (b) HTS coil using the NI winding technique.

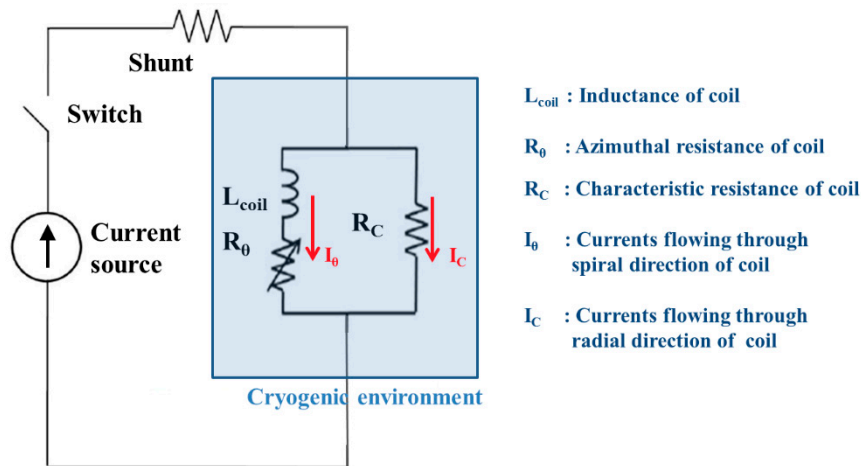


**Figure 2.** Simplified equivalent circuit model of the NI HTS coil.

Various researchers have attempted to apply HTS coils to electrical machines, such as motors and generators [26–33]. Specifically, these studies are more actively carried out in relation to electrical rotating machines, which require high output power levels, such as those used for wind power generation and in electric vehicle applications. Thus far, most studies on the application of superconducting coils to electrical rotating machines have mainly used an air-core type of structure, which does not use iron cores. In electrical rotating machines with an air-core structure, the superconducting field coils are positioned in the rotor to create a rotating field. Therefore, in the rotating field coil structure, the cooling system and the excitation system are inevitably complicated, and require a highly reliable design [31–34]. In the rotor excitation machine, the field current must be fed through the slip ring and brushes, and the cooling system requires dynamic seals for cryogenic transfer coupling. On the other hand, electrical rotating machines, such as a flux-switching machine (FSM), a homopolar machine and a Vernier machine, use iron cores, but it is possible to realize a robust machine, because they have stationary field coil structures. The cooling system and excitation system for the field coils in machines with a stationary field coil structure can be made simpler than those in a machine with a rotating field coil structure. For this reason, research on the application of HTS field coils to electrical rotating machines with a stationary field coil structure has been active. In particular, the FSM with stationary HTS field coils is becoming more attractive, given its advantages of a robust rotor and a reliable machine structure [32–38].

However, while the FSM has a robust rotor structure, the protection issue related to HTS field coils should be considered, as in other HTS rotating machines. The NI winding technique can serve

as a solution in this case. However, the FSM uses a ferromagnetic core to create a switched type of flux, which makes the inductance of the HTS field coil very large. Therefore, the intrinsic charging and discharging delay effect of the NI coil becomes very large. This can also develop into a technical problem during the application of an electrical rotating machine requiring flux-control capabilities. Therefore, in order to apply an NI HTS field coil to a flux-controllable FSM, a separate winding is required for flux regulation.

In this paper, the structure of an NI HTS FSM capable of flux control is proposed. An FSM applying the proposed structure was designed, and its flux regulation characteristics were analyzed through a transient motion analysis. To do this, an NI HTS field coil was fabricated and tested, and the characteristic resistance of the fabricated NI HTS field coil was calculated from the charging time constant through a current charging test of the coil. It was confirmed that the flux-control capability cannot be achieved by applying only the NI HTS fields for field excitation. Therefore, in order to realize the flux-control capabilities of the NI HTS FSM, a separate winding is required for flux regulation.

## 2. Machine Structure Operating Principle and Design of the Flux-Controllable NI HTS FSM

### 2.1. Machine Structure of the Flux-Controllable NI HTS FSM

Figure 3 shows the topology of the flux-controllable FSM proposed in this paper. It is composed of a rotor core, armature windings, NI HTS field coils, and additional field windings. All windings, including the field windings, are located in the stator core. Accordingly, the machine has a robust rotor structure. A ferromagnetic material is used for the stator and the rotor core. Three-phase armature windings are considered, and the armature windings are placed in each stator slot, with each winding connected in series. The NI HTS field coils generate the main magnetic flux during the steady-state operation, and additional field windings are used for flux regulation. Unlike conventional rotor excitation machines, the FSM has a doubly salient structure, with the field coils placed in the U-shaped iron core of the stator. In this machine, the rotor core has a simple laminated iron core which has salient poles. The flux direction of each field coil is opposite between the adjacent field coils.

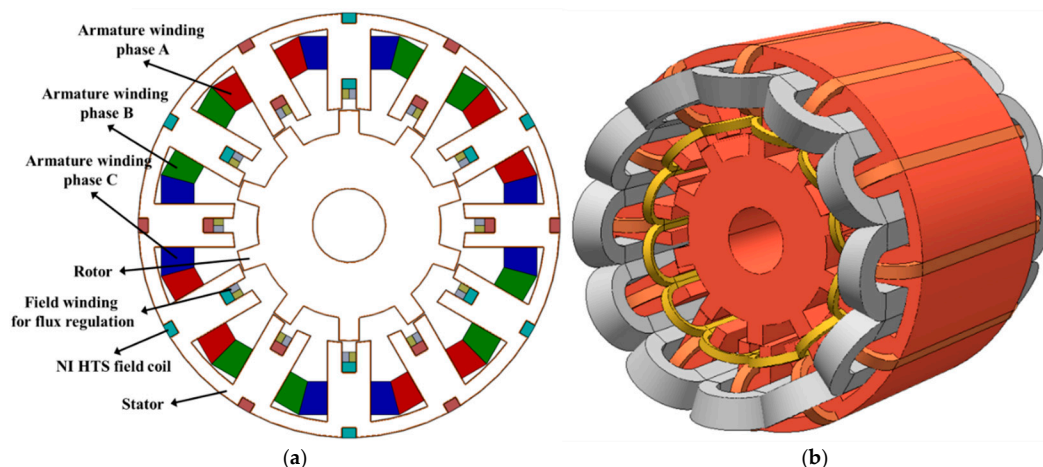


**Figure 3.** Topology of the flux-controllable flux-switching machine (FSM): (a) cross section, and (b) three-dimensional configuration.

### 2.2. Operating Principle of the Flux-Controllable NI HTS FSM

Figure 4 shows the principle of flux switching in the NI HTS FSM. With the doubly salient topology, the magnetic field generated by the NI HTS field coils always traverses the path with the minimum magnetic reluctance at positions where the rotor poles and the stator teeth are aligned to each other. At the rotor position shown in Figure 4a, the rotor pole aligns with one of two stator teeth, around which an armature winding is wound, and the magnetic flux that is linked in the armature winding, that



exits the rotor pole and enters the armature winding. When the rotor core rotates until another rotor pole aligns with the right part of the doubly salient pole of the stator, the magnetic flux goes out of the stator and into the rotor pole, maintaining the same amount of flux linkage, while reversing the polarity, thus ‘switching’ the flux. Clearly, as the rotor core rotates, the flux linkage in the armature windings will change periodically, inducing back-EMF.

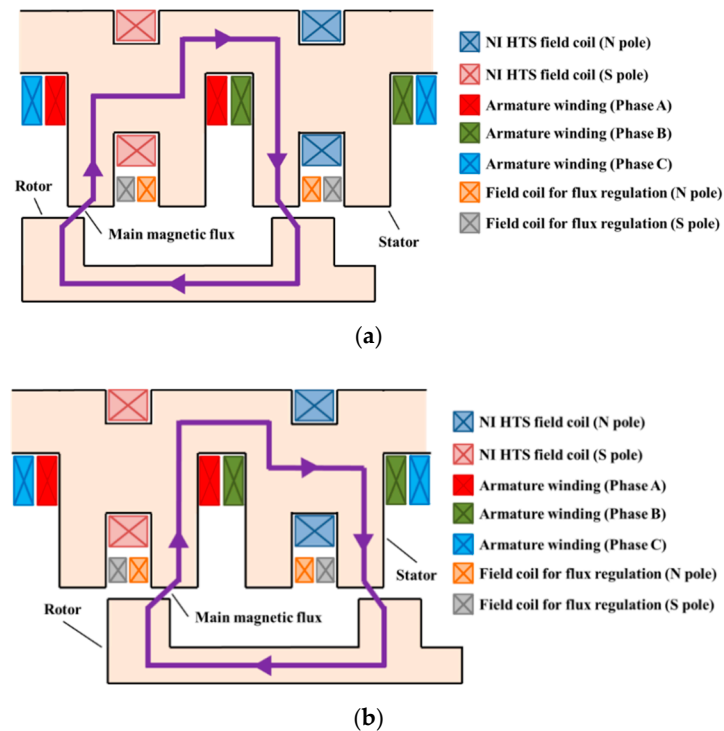


**Figure 4.** Operating principle: (a) starting point, and (b) after moving the rotor position by 180 electrical degrees.

Figure 5 represents the flux regulation principle of the flux-controllable FSM. In this machine, the flux-regulation capability is provided by additional field coils wound around the U-shaped doubly salient pole. Figure 5a shows the path of the main magnetic flux generated by the NI HTS field coil. Because the rotor tooth is aligned to the left of the doubly salient pole of the stator, the main magnetic flux forms a clockwise loop with the rotor tooth and the stator. Figure 5b presents the path of the magnetic flux generated by the additional field coil for flux regulation. The flux is generated by the additional field coil marked in yellow in the figure, and the flux also flows in the opposite direction when the direction of the field current changes. As the magneto-motive force (MMF) generated from the additional field coil increases, the flux-regulating effect is enhanced. If the direction of the magnetic flux generated by the additional field coil is identical to the direction of the main magnetic flux, the total magnitude of the flux linkage in the armature windings increases, and vice versa. Figure 5c shows an example of negative regulation, during which the amplitude of the flux linkage in the armature windings decreases.

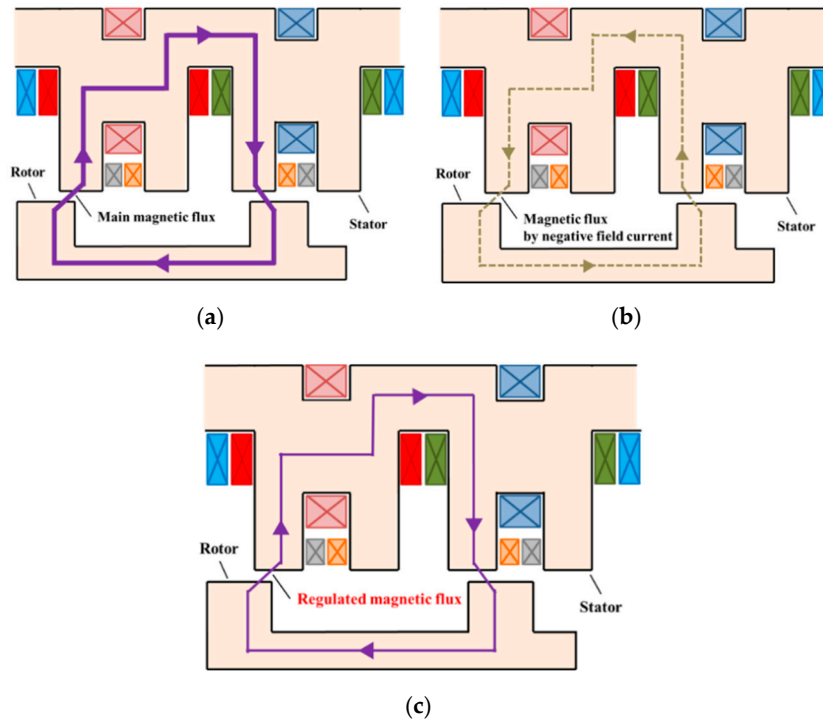


**Figure 5.** Flux regulation principle: (a) main magnetic flux by the NI HTS field coil, (b) magnetic flux by the additional field coil, and (c) regulated magnetic flux.

### 2.3. Design of the Flux-Controllable FSM

In this study, a three-phase FSM with a rated output power of 20 kW, and a rotation speed of 1000 rpm, was considered. The design was carried out through the following process [32,33].

1. The design specifications of the NI HTS FSM, in this case the output power, flux regulation ratio and phase, are determined.
2. The maximum radius  $r_{r,max}$  and length  $l_{max}$  of the rotor are calculated considering rotor material's mechanical properties, using Equations (1) and (2), respectively.

$$r_{r,max} = \sqrt{4\sigma_{yield} / ((3 + \nu)\rho\Omega^2)} \tag{1}$$

$$l_{max} = \sqrt{\pi^2 / k\Omega \sqrt{EI / \rho S}} \tag{2}$$

3. The slot pitch is calculated based on the pole pitch and the numbers of slots. The number of conductors also are calculated using Equation (3).

$$S_{slot} = S_{Cu} \cdot n_0 / \beta = I_0 \cdot n_0 / (J_{Cu} \cdot \beta) = d_{slot} \cdot w_{slot} \tag{3}$$

4. The dimensions of the armature conductor and the slot are determined by Equation (4).

$$d_{Cu} = 2 \cdot d_{slot} \cdot \sqrt{\beta} / n_0, w_{Cu} = w_{slot} \cdot \sqrt{\beta} / 2 \tag{4}$$

5. The tangential stress in the rotor is calculated using the rotor dimension and the torque via Equation (5).

$$\sigma_{Ftan} = T / (2\pi r^2 l) \tag{5}$$

6. The required air-gap field density,  $B_0$ , is then calculated by Equation (6).

$$B_0 = \sqrt{2\pi\sigma_F \tan(2r)} / (I_S n_0 q \cos \varphi) \quad (6)$$

7. Based on the required flux regulation ratio and  $B_0$ , the NI HTS field coil and the additional field winding are designed by means of FEM under a no-load condition.
8. The cryostat for the NI HTS field coil is designed based on the HTS field coil and other thermal loads. The thermal loads of the cryostat are calculated by the equations below [39–41].

$$Q_{CL} = (\sqrt{P_{CL} I_{CL}^2 / A_{CL}} - \sqrt{k_{CL} A_{CL} (T_H - T_L) / L_{CL}})^2 + 2I \sqrt{\rho_{CL} k_{CL} (T_H - T_L)} \quad (7)$$

$$Q_K = N_L A_L k_L (T_H - T_L) / L_L \quad (8)$$

$$Q_R = \sigma (T_H^4 - T_L^4) / ((1 - \varepsilon_H) / \varepsilon_H A_H + (1 / \varepsilon_L + 2N / \varepsilon_N - N) / A_L) \quad (9)$$

Here,  $Q_{CL}$ ,  $Q_K$ , and  $Q_R$  are the thermal loads from the conduction heat transfers by a pair of current leads, the leading-in tubes for the signal lines, and the radiation heat transfer.

9. Characteristic analyses of the deigned machine are carried out in the form of a transient motion analysis, using a commercialized FEM software package.

In this design, an NI HTS field coil was considered for field excitation. Therefore, the characteristic resistance,  $R_C$ , of the NI HTS field coil is required as a design parameter. For this reason, an NI HTS field coil was fabricated to obtain an  $R_C$  value. The  $R_C$  value can be calculated from a charging time constant ( $\tau$ ) by a charging test. Figure 6 shows the NI HTS field coil fabricated in this study. The HTS coil was fabricated using 2G HTS wire with a 12 mm width. It has a double-layered structure with 40 winding turns. Both the effective length and width of the G10 bobbin for the NI HTS coil are 600 mm and 150 mm, respectively. Table 1 shows the specifications of the NI HTS field coil. To determine the characteristic resistance of the fabricated NI HTS field coil, the current charging test was carried out in liquid nitrogen. Figure 7 shows the normalized central magnetic field after current charging at 100 A, with a cryogenic Hall sensor used to measure the magnetic field. After the power supply current reached the target current of 100 A, the magnetic field relaxes over time while holding the current. The field increases logarithmically to approximately 25 mT at 600 s. This outcome indicates that the fabricated NI HTS field coil is affected by the charging delay phenomenon. The typical method for calculating  $R_C$  in NI HTS coils is to use a decay time constant after a sudden discharge of the power supply current. However,  $R_C$  for the straight section in a racetrack coil depends on the Lorentz force induced by the excitation current. Because the Lorentz force dissipates as the coil current is instantly decreased to zero,  $R_C$  is not at all affected by the Lorentz force during a sudden charge [32,42]. Therefore, it is more appropriate to calculate the  $R_C$  of the NI HTS racetrack coil using the charge time constant. The charging time constant,  $\tau$ , can be defined as the time interval between  $B_1$  and  $B_2$  in Figure 7, where  $B_1$  is the magnetic field density at the moment when the power supply current is fully charged, and  $B_2$  is the sum of  $B_1$  and  $B$ , which is 0.63 between  $B_1$  and a fully charged level.

In Figure 7, the charging time constant ( $\tau$ ) is 89.34 s. The  $R_C$  value of the coil calculated from the charging time constant is 145  $\mu\Omega$ . Here,  $L$  and  $\tau$  are the coil inductance and the time constant, respectively. Figure 8 shows the measured results of the magnetic field distribution in the NI HTS field coil measured at an excitation current of 100 A. For this measurement, a field mapper with a three-axis motor for sensor movements was used. Considering the charging delay phenomenon of the NI HTS field coil, the magnetic field distribution measurement was performed after 800 s. As indicated in the graph, the central magnetic field generated from the NI HTS field coil at an excitation current of 100 A is 25 mT, and the magnetic field density increases toward the coil winding part.

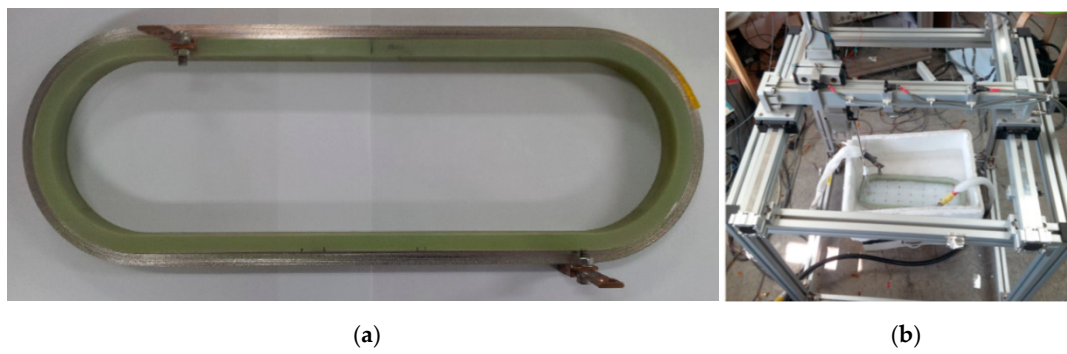


Figure 6. (a) Pictures of the fabricated NI HTS field coil, and (b) test set-up.

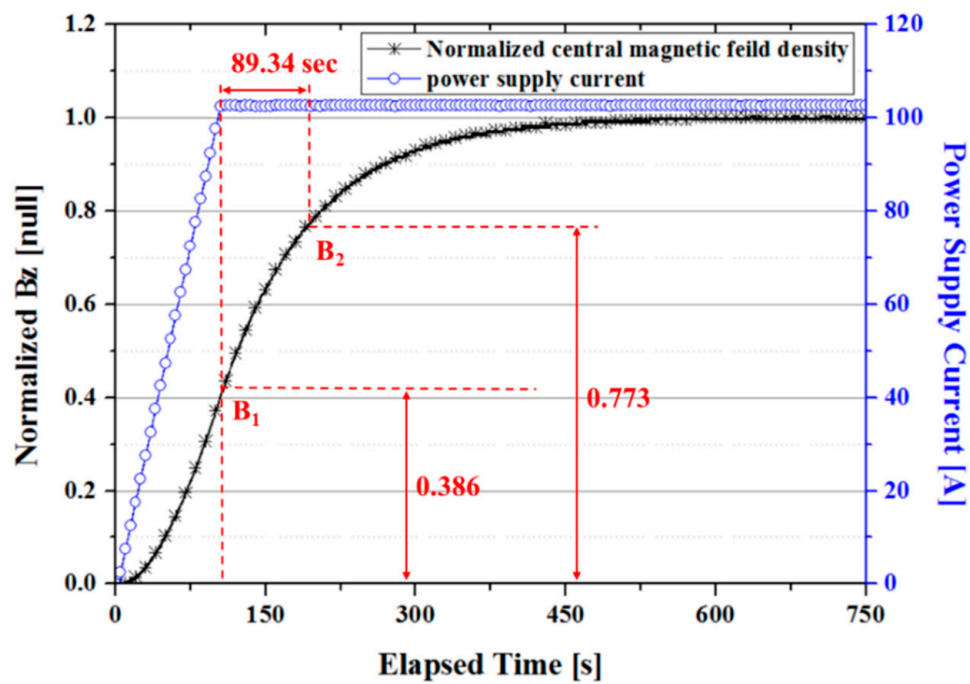


Figure 7. Charging test result of the fabricated NI HTS field coil.

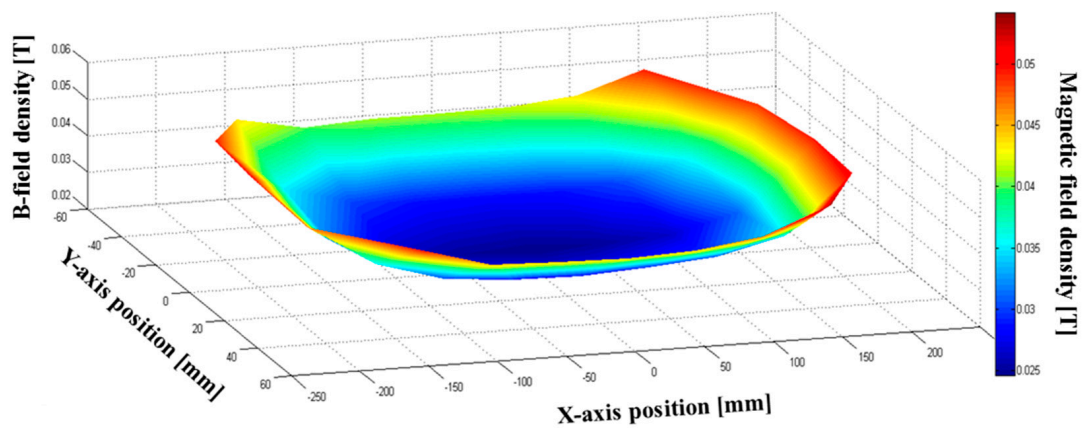


Figure 8. Measured magnetic field distribution of the fabricated NI HTS field coil.

**Table 1.** Key Parameters of the NI HTS Field Coil.

Item	Value
2G HTS wire	2G HTS wire manufactured by AMSC
Wire width	12 mm
Winding structure	Racetrack and single pancake
Length of the straight coil part	600 mm
Inner radius of the coil end part	65 mm
Total winding turns	40
Insulation type	No-insulation
Inductance	1.3 mH
Operating temperature	77 K
Nominal operating current	100 A

Based on the aforementioned design process, an NI HTS FSM with a 12-tooth stator was initially chosen. Table 2 presents the design parameters of the NI HTS FSM. A liquid nitrogen cryostat, a vacuum-layered cryostat with a pair of current leads, a liquid nitrogen inlet, a liquid nitrogen outlet, and leading-in tubes, were designed. In order to account for the radiation heat loss, multi-layer insulation (MLI) in the vacuum layer was considered. According to Equations (7)–(9), the total heat loss for each cryostat was calculated and found to be approximately 15 W when three layers of MLI were inserted into the vacuum space. Figure 9 shows the designed LN<sub>2</sub> cryostat.

**Table 2.** Key Design Parameters of the FSM.

Item	Value
Maximum output power	36 kW
Phases	3
Rotating speed	1000 rpm
Stator inner diameter	563 mm
Air-gap distance	3 mm
Rotor inner diameter	175 mm
Active stack length	600 mm
No. of stator slots	12
No. of rotor poles	10
Stator tooth arc	7.5°
Slot arc	8.25°
Winding turns per armature coil	12
No. of field coils for flux regulation	12
Winding turns per field coil for flux regulation	20

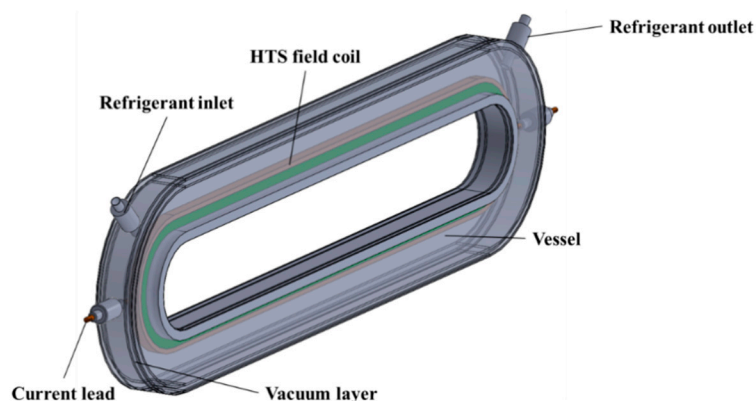


**Figure 9.** Liquid nitrogen (LN<sub>2</sub>) cryostat for the NI HTS field coil.



### 3. Characteristic Analysis of the Flux-Controllable NI HTS FSM

#### 3.1. Field Distribution of the Proposed FSM

In this study, the operating characteristics of the designed NI HTS FSM were analyzed by a combination of the finite element method (FEM) and an electrical circuit analysis. The electrical circuit model was devised based on the simplified circuit model shown in Figure 2. The  $R_C$  value in the electrical circuit model was calculated from the current charging test of the NI HTS coil. Simulations were performed using FEM software, and the electrical circuit was modeled using a circuit modeler, and was simulated by interworking with the electromagnetic analysis, as shown in Figure 10. In this model, the azimuthal resistance of the HTS coil is assumed to be zero. Figure 11 presents the simulation results of the current charging characteristics of the NI HTS field coil under a 100 A field current with a ramping rate of  $1 \text{ A s}^{-1}$ . The charging time constant,  $\tau$ , can be calculated from the time interval between  $I_1$  and  $I_2$  in Figure 11, as in NI HTS field coil test, because the magnetic field density is proportional to the coil current. Here,  $I_1$  is the coil current at the moment when the power supply current reaches the target, and  $I_2$  (66.48 A) represents the sum of  $I_1$  and  $I$ , which is 63% (57.08 A) between  $I_1$  (9.40 A) and a fully charged coil current (100 A). The value of  $\tau$  is 608 s. The coil current is fully charged approximately 9500 s after the excitation current reaches the target. Therefore, the initial time for the simulations of the designed NI HTS FSM in the steady-state condition was set to 10,000 s, considering a full charge of the field current. Figure 12 shows the magnetic flux vector at the rotor position of 0 degrees and 15.75 degrees 10,000 s after the field current reaches the target of 100 A.

The simulation results show that the polarity of the magnetic flux applied to the armature winding changes as the rotor moves. Figure 13 shows the air-gap flux density distributions due only to the excitation of the NI HTS field coils. The local maximum value of the air-gap flux density appears at the position where the stator tooth is fully overlapped with the rotor pole. The local maximum value directly results in the maximum flux of the armature winding  $A_1$ , and thus is more representative than the absolute maximum value [43]. Therefore, flux regulation can be achieved effectively by adjusting the local maximum value.

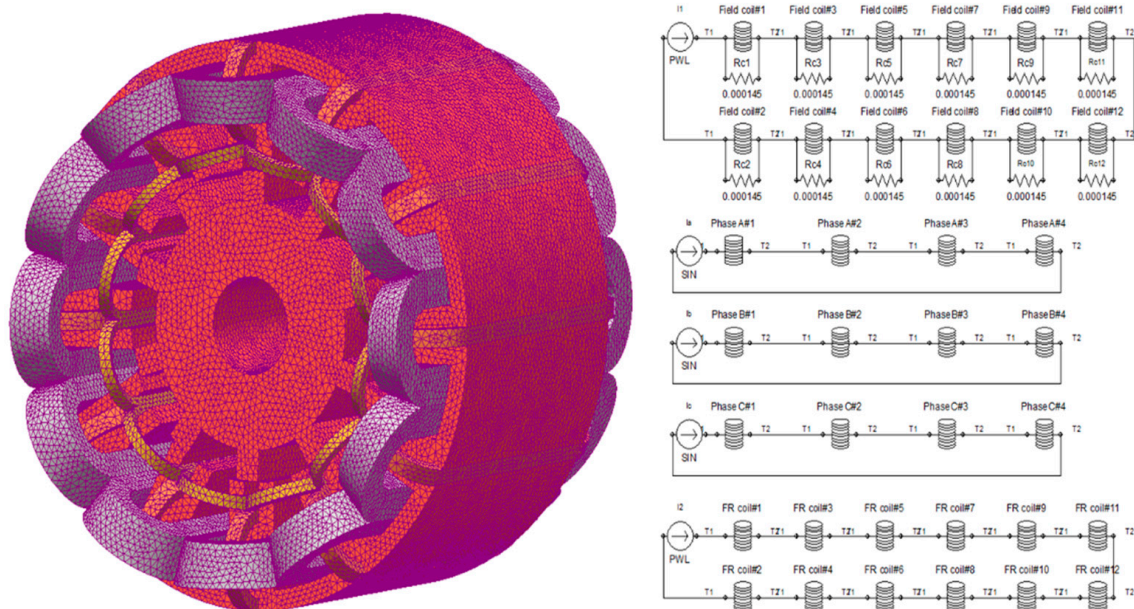


Figure 10. Field-circuit coupled finite element method (FEM) model of the designed NI HTS FSM.

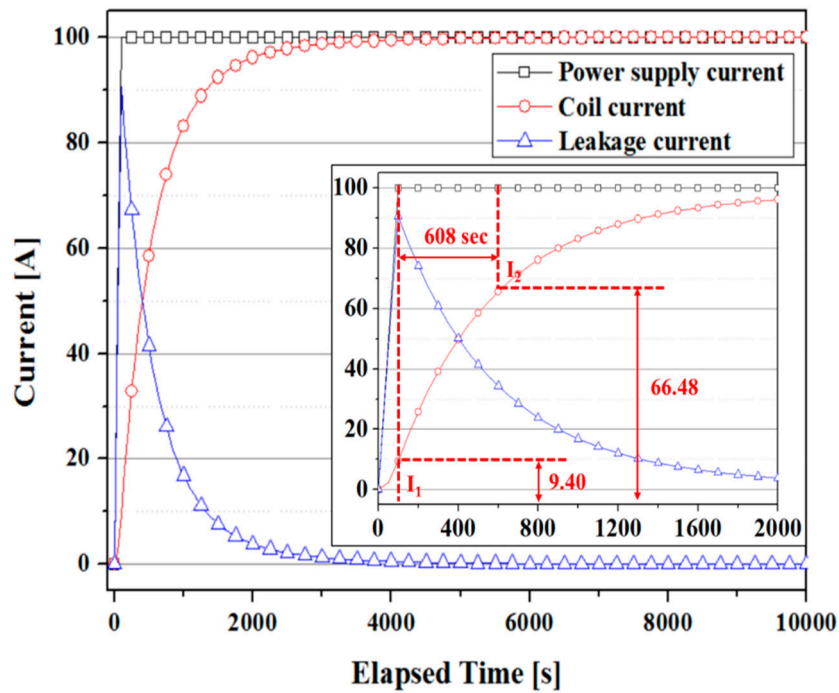


Figure 11. Current charging characteristics of the NI HTS field coil installed in the designed FSM.

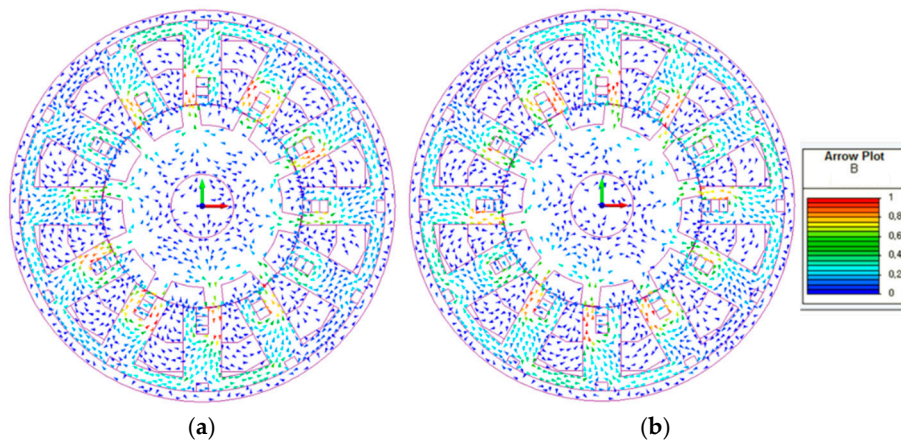


Figure 12. Magnetic flux density vector plots according to the rotor position: (a) 0°, and (b) 15.75°.

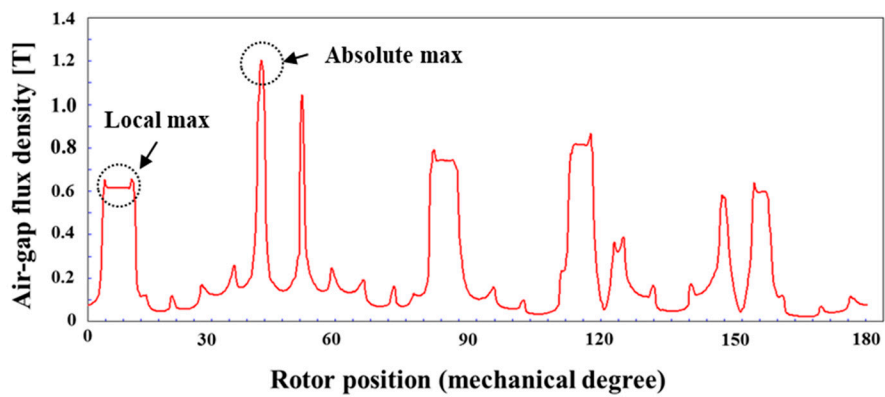


Figure 13. Air-gap flux density distribution due only to the excitation of the NI HTS field coils when the rotor position is on the d-axis.

### 3.2. Operating Characteristics of the Proposed FSM Due Only to NI HTS Field Coil Excitation

In this study, the operating characteristics of the NI HTS FSM were analyzed when excited only with the HTS field coil. Figure 14 presents the flux linkage waveform of the three-phase armature windings. The excitation current of the NI HTS field coil in this analysis is 100 A, and the rotation speed of the rotor is 1000 rpm. In this graph, the  $x$ -axis represents the elapsed time 10,000 s after the coil current reaches 100 A. As shown in Figure 14, the flux linkage waveforms are nearly sinusoidal, and the peak value of the flux linkage is close to 0.6 Wb. Figure 15 shows the no-load voltage waveforms of three-phase armature windings. The peak value of the no-load voltage is approximately 770 V. The no-load voltage waveforms exhibit harmonics components due to the lower saturation degree and the rough comparison to conventional machines. The roughness is due to the shield effect of the NI coils. Figure 16 shows the waveforms of the phase voltage and line current in the unit-load condition. The current and voltage waveforms are nearly sinusoidal. From the data shown in Figure 16, it is confirmed that the output power is 20 kW.

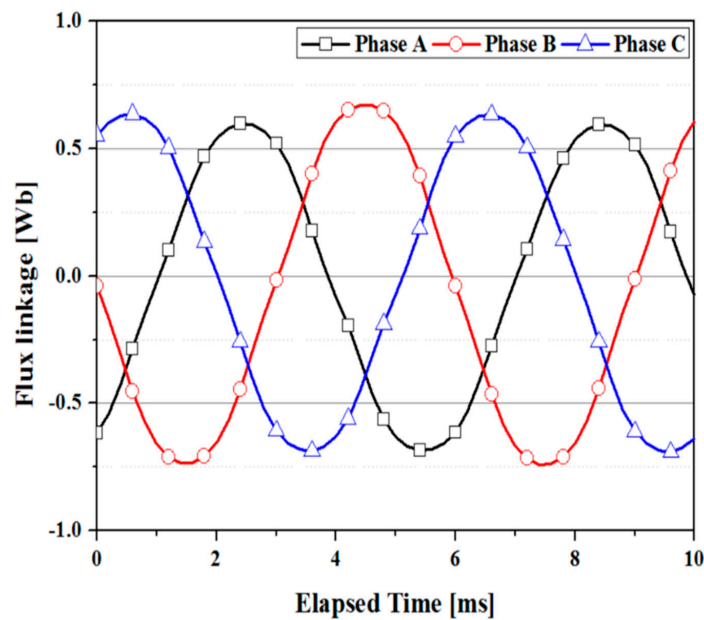


Figure 14. Flux linkage due only to the NI HTS field coil.

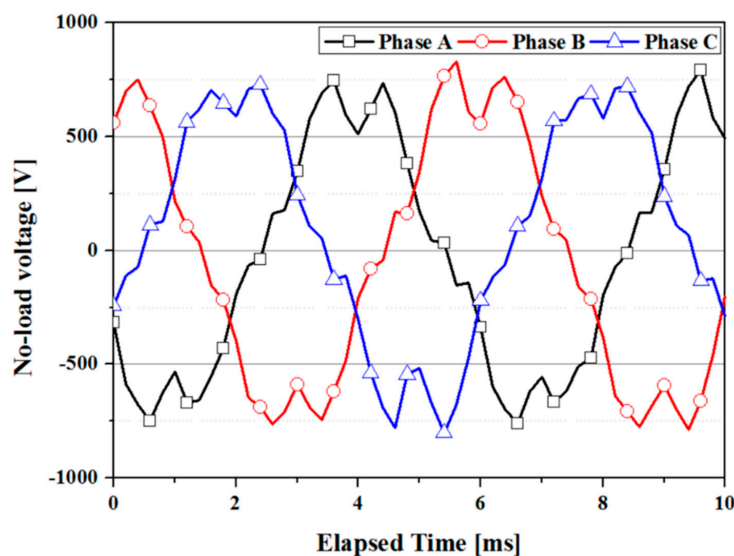
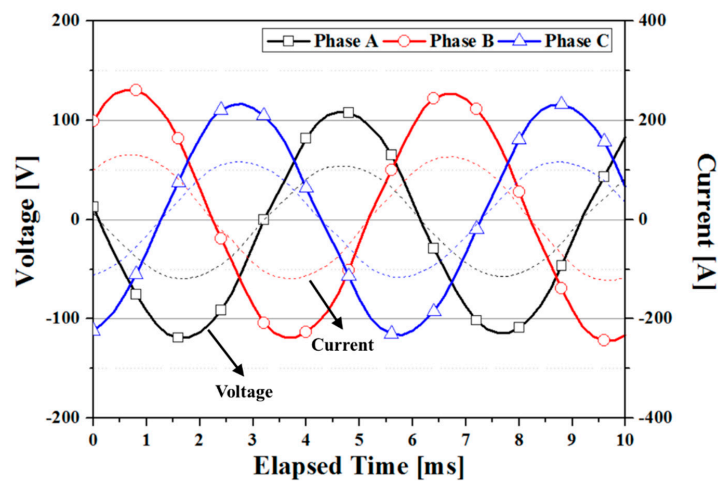


Figure 15. No-load voltage due only to the NI HTS field coil.



**Figure 16.** Phase voltage and line current in resistance-load condition due only to the NI HTS field coil.

### 3.3. Flux-Regulation Characteristics of the Proposed FSM

The flux-regulation characteristics were analyzed by means of a transient motion analysis. With the FEM, the no-load magnetic field distributions and flux contours of the proposed machine with different MMF levels of the additional field windings were analyzed. Figure 17 shows the magnetic field distributions according to the MMF of the additional field windings. In this analysis, the excitation current of the NI HTS field coil was maintained at 100 A, while the MMF of the additional field winding was changed. Figure 17c presents the magnetic field distribution and flux contour under only NI HTS field coil excitation. Figure 17a,b show the field distributions with negative regulation current levels of 20 A and 10 A, respectively. Correspondingly, Figure 17d,e show the field distributions with positive regulation current levels of 20 A and 10 A. These figures show that as the regulation current increases, the magnitude of the magnetic field density in the FSM also increases.

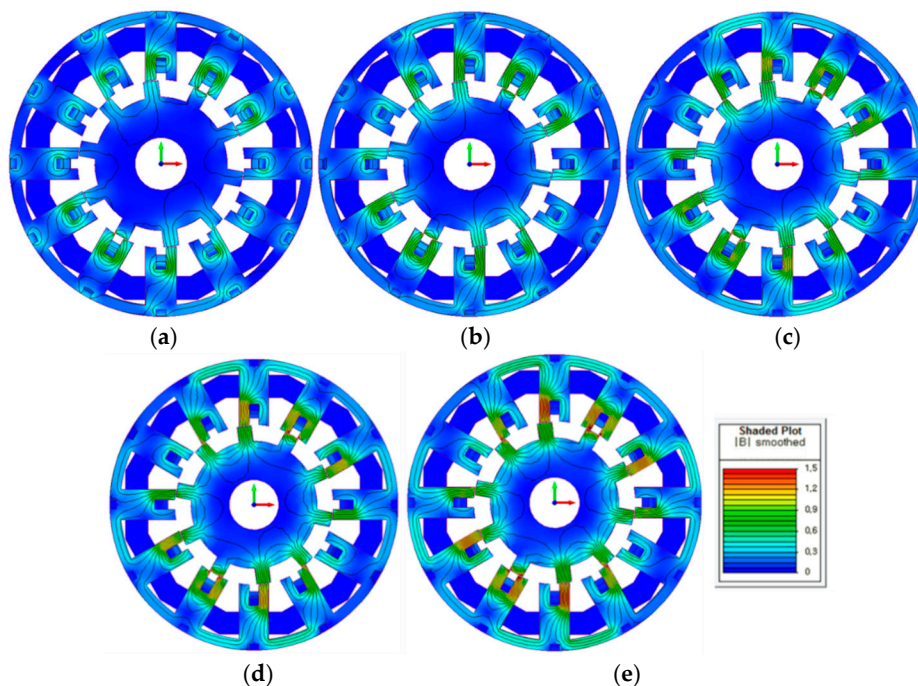


**Figure 17.** Flux vector contour and magnetic field distribution according to the magneto-motive force (MMF) of the additional field winding: (a)  $-4 \text{ kA}\cdot\text{T}$ , (b)  $-2 \text{ kA}\cdot\text{T}$ , (c)  $0 \text{ kA}\cdot\text{T}$ , (d)  $2 \text{ kA}\cdot\text{T}$ , and (e)  $4 \text{ kA}\cdot\text{T}$ .



Figure 18 shows the flux linkage of the phase C armature winding under different regulation current levels. The regulation current was maintained at zero until 14 milliseconds, and the regulation current was applied to the additional field winding after 14 milliseconds. By controlling the regulation current, the flux linkage of the armature winding can be regulated. When the NI HTS field coils and additional field windings work together, a flux-regulation operation is achieved. Figure 19 compares the no-load voltage waveforms under different regulation modes at 1000 rpm. For solely the NI HTS field coil excitation mode, the peak value of the no-load voltage is approximately 770 V. The peak values in the maximum negative regulation current, and the positive regulation current, are 410 and 980 V, respectively. By applying MMF of  $-20 \text{ kA}\cdot\text{T}$ , the amplitude of the no-load voltage can be reduced by nearly 53%, from 770 V to 410 V. By applying MMF of  $20 \text{ kA}\cdot\text{T}$ , the amplitude of the no-load voltage can be increased by 27%, from 770 V to 980 V. Figures 20 and 21 correspondingly show the phase voltage and phase current waveforms at the rated operation condition. In this case, the armature winding coils were connected to a resistance load. The simulation results confirm that the output power of the FSM in the negative regulation mode can be reduced to approximately 6.7 kW. On the other hand, in the positive regulation mode, the output power of the FSM is approximately 36.2 kW, which is increased by 180%, compared to that in the solely NI HTS field coil excitation mode. Figure 22 shows the torque curve according to the MMF of the additional field winding. From these simulation results, it is confirmed that the torque of the machine in the positive regulation mode is approximately 4700 N·m, which is increased by 210%, compared to that of the solely NI HTS field coil excitation mode.

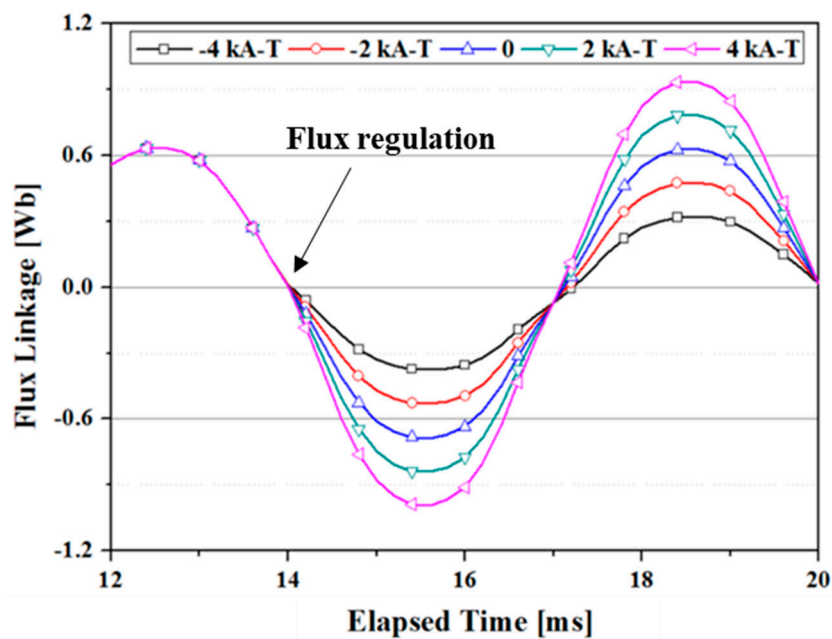


Figure 18. Flux linkage of Phase C according to the MMF of the additional field winding.



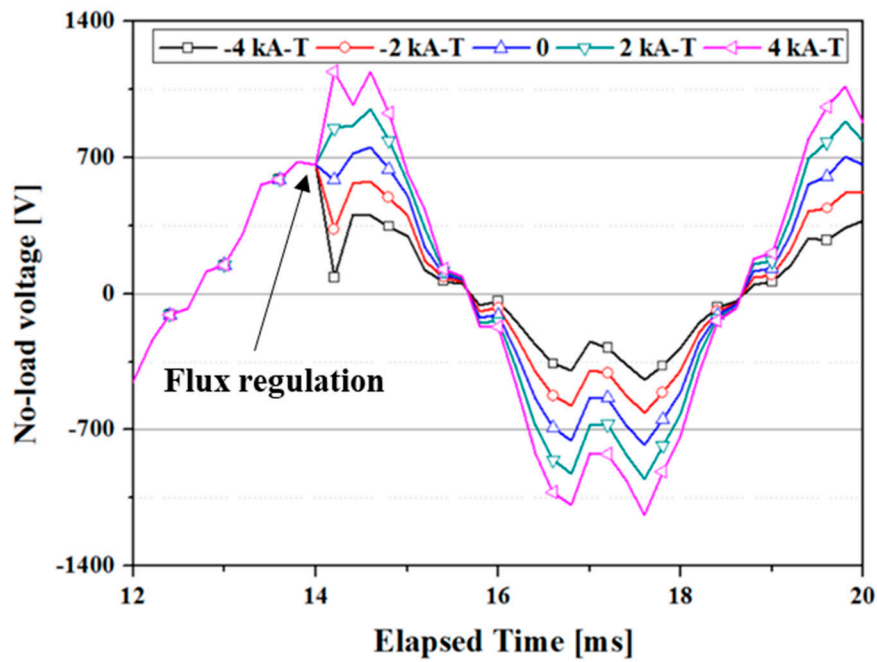


Figure 19. No-load voltage of Phase C according to the MMF of the additional field winding.

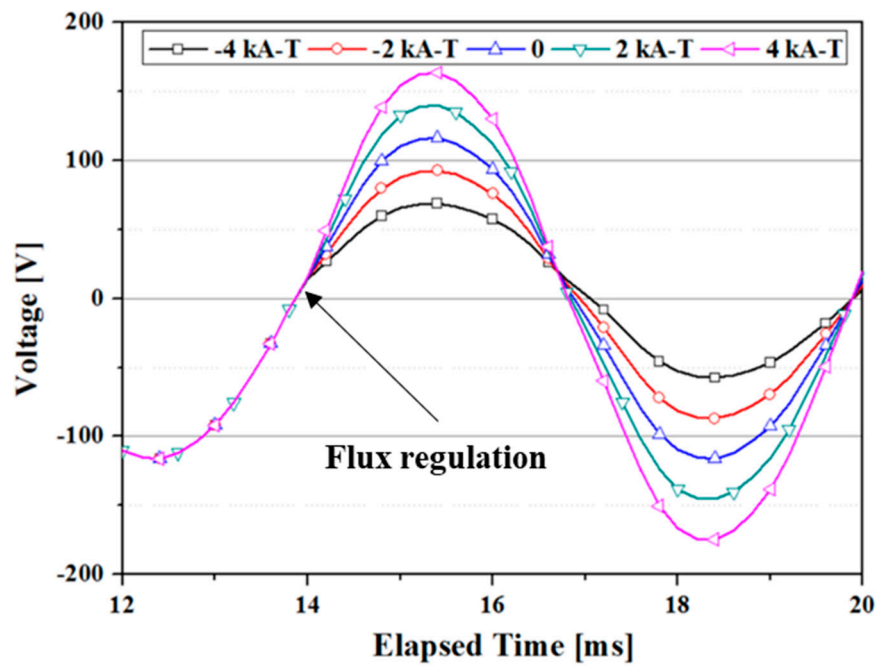


Figure 20. Phase voltage of Phase C in the resistance-load condition according to the MMF of the additional field winding.

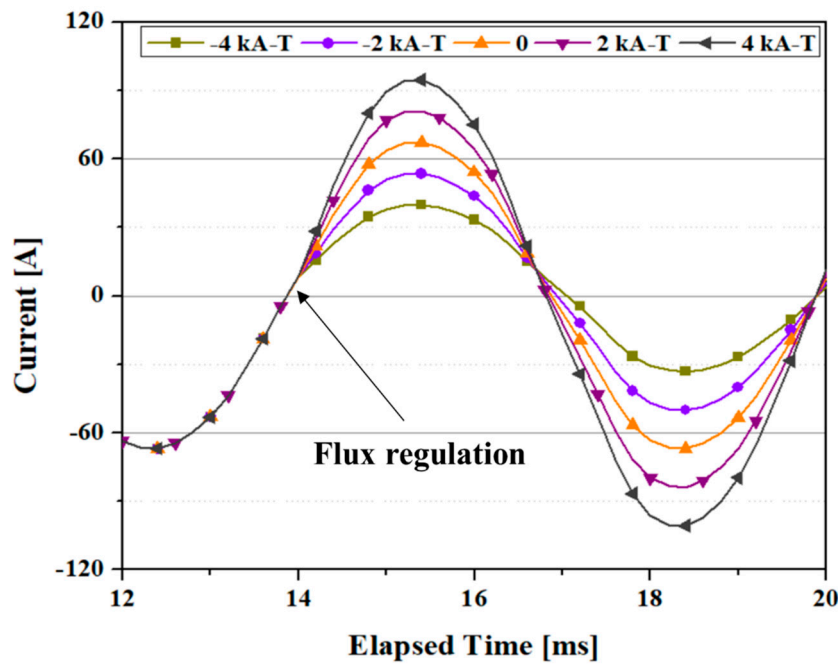


Figure 21. Phase current of Phase C in the resistance-load condition according to the MMF of the additional field winding.

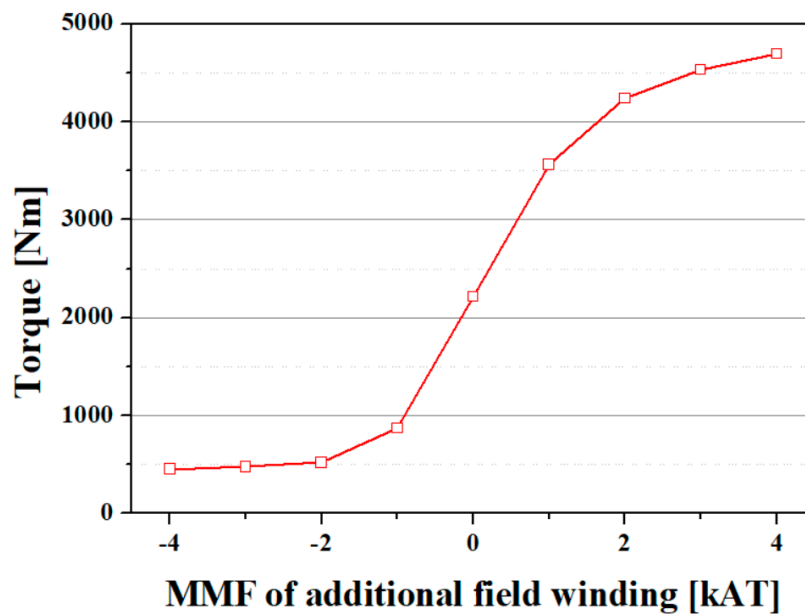


Figure 22. Torque curve according to the MMF of the additional field winding.

#### 4. Discussion

This paper deals with a flux-controllable NI HTS flux-switching machine (FSM) for electric vehicle (EV) applications. In a variable-speed rotating machine for EVs, flux-regulation capabilities are very important for constant output operation. Conventional HTS rotating machines have excellent flux-regulation capabilities, but for an HTS rotating machine using no-insulation (NI) HTS field coils, ensuring flux-regulation capabilities is difficult, due to their inherent charge and discharge delays. However, the NI winding technique can dramatically improve the operational stability of HTS field coils. Therefore, research to implement an HTS rotating machine with flux-regulation capabilities,

while improving the operating stability of the HTS field coil via the NI winding technique, is required for EV applications.

In this paper, we propose an HTS rotating machine with a flux switching structure and an NI HTS field coil. The proposed NI HTS flux-switching machine (FSM) uses additional windings for flux regulation, which enables feasible flux control. In addition, an NI HTS field coil was fabricated and tested, because the characteristic resistance,  $R_C$ , of the NI HTS field coil is required as a design parameter. Based on the  $R_C$  value of the fabricated NI HTS field coil, an NI HTS FSM was designed, and the flux-regulation performance outcomes were analyzed. The flux-regulation performance capabilities were analyzed using a combination of the finite element method (FEM) and an electrical circuit analysis. The electrical circuit model was devised based on the equivalent circuit model of the NI HTS coil. The simulation results showed that the charging time constant ( $\tau$ ) of the NI HTS FSM is 608 s, and that the coil current becomes fully charged approximately 9500 s after the excitation current reaches the target. This means that the HTS FSM using NI HTS field coils cannot control the flux by adjusting the field current of the HTS field coil. Therefore, additional windings are required for the flux control of the NI HTS FSM. In a simulation of the model with additional windings for flux regulation, the flux linkage and back-EMF characteristics, the output characteristics under a resistance load, and the torque characteristics of the proposed machine, were investigated. The simulation results demonstrated that the NI HTS FSM is capable of effective flux-regulation performance, enabling power and torque regulation. However, further research on the applicability of the proposed NI HTS FSM is needed, with the fabrication and testing of prototype models.

## 5. Conclusions

In this paper, a novel flux-controllable NI HTS flux-switching machine (FSM) for electric vehicle applications was proposed. This topology makes the NI HTS FSM more attractive, because it improves the flux-regulation capabilities. The proposed machine adopts both NI HTS field coils and additional windings. The proposed HTS flux-switching machine (FSM) uses NI field coils, but additional field windings are applied for flux regulation, which enables good flux control. An NI HTS field coil was also fabricated and tested. The characteristic resistance of the NI HTS field coil was obtained from a current charging test of the coil. The characteristic resistance was used for the design and in a characteristic analysis of the NI HTS FSM. To analyze the flux-regulation performance capabilities of the NI HTS FSM, a simulation model including an electrical circuit was devised based on the characteristic resistance of the fabricated NI HTS field coil. This study shows that flux-regulation capabilities can be realized through the proposed structure, even in the NI HTS FSM. The results here also provide a good reference for those involved in the manufacturing of a prototype NI HTS FSM for EV applications, and they can also be used as a reference for other HTS rotating machines, such as those used in association with large-scale wind power generation.

**Author Contributions:** All authors contributed to this work by collaboration. Conceptualization, Y.J.H.; Formal analysis, Y.J.H.; Methodology, Y.J.H.; Supervision, Y.J.H.; Supervision, Y.J.H.; Writing-original draft, Y.J.H.; Visualization, J.Y.J.; Validation, J.Y.J.; Writing-review & editing, S.L. All authors have read and agree to the published version of the manuscript.

**Funding:** This work was funded by the Korea Basic Science Institute under Grant D010200.

**Acknowledgments:** This work was supported by the Korea Basic Science Institute under Grant D010200.

**Conflicts of Interest:** The authors declare no conflict of interest.

## Nomenclature

$\sigma_{yield}$	yield strength
$\nu$	Poisson's ratio
$\rho$	density of the rotor material
$n_0$	number of armature conductors per slot
$I_0$	total current per slot
$r$	outer radius of the rotor
$l$	effective length of the rotor
$\Omega$	mechanical angular speed
$E$	Young's modulus
$k$	safety factor
$S_{Cu}$	cross-sectional area of the armature conductor
$J_{Cu}$	the allowable current density of the armature conductor
$d_{slot}$	slot height
$w_{slot}$	slot width
$d_{Cu}$	armature conductor height
$w_{Cu}$	armature conductor width
$\beta$	packing factor
$P$	rated output power
$\sigma_{Ftan}$	tangential stress of the rotor
$T$	torque of the rotor
$I_S$	RMS value of the phase current
$q$	number of the slots
$\cos \varphi$	power factor
$\rho_{cl}$	electrical resistivity of the current lead
$l_{cl}$	length of the current lead
$I$	transport current through the current lead
$A_{cl}$	cross-sectional area of the current lead
$k_{cl}$	thermal conductivity of the current lead
$T_H$	temperature at the high-temperature part
$T_L$	temperature at the low-temperature part
$N_l$	no. of signal lines or leading-in tubes
$A_l$	cross-sectional area of a signal line or a leading-in tube
$k_l$	thermal conductivity of a signal line or a leading-in tube
$L_l$	length of a signal line or a leading-in tube
$\sigma$	Stefan–Boltzmann constant ( $5.67 \times 10^{-8} \text{ W}\cdot\text{m}^{-2}\cdot\text{K}^{-4}$ )
$\varepsilon_H$	emissivity of the vessel
$\varepsilon_N$	emissivity of MLI
$N$	no. of MLI layers
$A_H$	surface area of the high-temperature part
$A_L$	surface area of the low-temperature part

## References

1. Ehsani, E.; Gao, Y.; Miller, J.M.; John, M.M. Hybrid electric vehicles: Architecture and motor drives. *Proc. IEEE* **2007**, *4*, 719–728. [[CrossRef](#)]
2. Chan, C.C.; Chau, K.T. An overview of power electronics in electric vehicles. *IEEE Trans. Ind. Electron.* **1997**, *44*, 3–13. [[CrossRef](#)]
3. Gao, D.W.; Mi, C.; Emadi, A. Modeling and simulation of electric and hybrid vehicles. *Proc. IEEE* **2007**, *95*, 729–745. [[CrossRef](#)]
4. Chau, K.T.; Chan, C.C. Electric vehicle technology - a timely course for electrical engineering students. *Int. J. Electr. Eng. Educ.* **1998**, *35*, 212–220. [[CrossRef](#)]
5. Okura, K. Development and future issues of high voltage systems for FCV. *Proc. IEEE* **2007**, *95*, 790–795. [[CrossRef](#)]

6. Chau, K.T.; Wong, Y.S.; Chan, C.C. An overview of energy sources for electric vehicles. *Energy Convers. Manag.* **1999**, *40*, 1021–1039. [[CrossRef](#)]
7. Chau, K.T.; Wu, K.C.; Chan, C.C.; Shen, W.X. A new battery capacity indicator for nickel-metal hydride battery powered electric vehicles using adaptive neuro-fuzzy inference system. *Energy Convers. Manag.* **2003**, *44*, 2059–2071. [[CrossRef](#)]
8. Sekiguchi, D.; Nakamura, T.; Misawa, S.; Kitano, H.; Matsuo, T.; Amemiya, N.; Ito, Y.; Yoshikawa, M.; Tezawa, T.; Osamura, K.; et al. Trial Test of Fully HTS Induction/Synchronous Machine for Next Generation Electric Vehicle. *IEEE Trans. Appl. Supercond.* **2012**, *22*, 5200904. [[CrossRef](#)]
9. Shinzato, T.; Arakawa, S.; Oyama, H.; Saka, H.; Hayasaki, T. Development of High-Temperature Superconducting Motor for Automobiles. *SEI Tech. Rev.* **2012**, *75*, 62–65.
10. Oyama, H.; Shinzato, T.; Kitajima, K.; Hayashi, K. Application of Superconductors for Automobiles. *SEI Tech. Rev.* **2008**, *67*, 22–26.
11. Nakamura, T.; Itoh, Y.; Yoshikawa, M.; Nishimura, T.; Ogasa, T.; Amemiya, N.; Ohsashi, Y.; Fukui, S.; Furuse, M. Tremendous Enhancement of Torque Density in HTS Induction/Synchronous Machine for Transportation Equipments. *IEEE Trans. Appl. Supercond.* **2015**, *25*, 1–4. [[CrossRef](#)]
12. Masson, P.J.; Soban, D.S.; Upton, E.; Pienkos, J.E.; Luongo, C.A. HTS motors in Aircraft Propulsion: Design Considerations. *IEEE Trans. Appl. Supercond.* **2005**, *15*, 2218–2221. [[CrossRef](#)]
13. Haran, K.S.; Kalsi, S.; Arndt, T.; Karmaker, H.; Badcock, R.; Buckley, B.; Haugan, T.; Izumi, M.; Loder, D.; Bray, J.W.; et al. High power density superconducting rotating machines—development status and technology roadmap. *Supercond. Sci. Technol.* **2017**, *30*, 123002. [[CrossRef](#)]
14. Hata, R.; Isojima, S. The Road to Liquid Hydrogen Electric Vehicle Powered by High-Temperature Superconducting Motor. *SEI Tech. Rev.* **2009**, *69*, 25–35.
15. Li, W.; Ching, T.W.; Chau, K.T.; Lee, C.H.T. A Superconducting Vernier Motor for Electric Ship Propulsion. *IEEE Trans. Appl. Supercond.* **2018**, *28*, 52010706. [[CrossRef](#)]
16. Kim, Y.-G.; Hahn, S.; Kim, K.L.; Kwon, O.J.; Lee, H. Investigation of HTS racetrack coil without turn-to-turn insulation for superconducting rotating machines. *IEEE Trans. Appl. Supercond.* **2011**, *22*, 5200604.
17. Kim, H.-W.; Jo, Y.-S.; Kim, S.-W.; Kim, H.M.; Jeong, J.-S.; Hong, J.-P.; Hur, J. Determining the Operating Current of No-Insulation Field Coils in HTS Generators. *IEEE Trans. Appl. Supercond.* **2015**, *51*, 9000404. [[CrossRef](#)]
18. Hwang, Y.J.; Ahn, M.C.; Lee, T.S.; Lee, W.S.; Ko, T.K. Experimental study of the effects of alternating fields on HTS coils according to the winding insulation conditions. *Supercond. Sci. Technol.* **2013**, *26*, 085021. [[CrossRef](#)]
19. Kim, K.L.; Choi, Y.H.; Yang, D.G.; Song, J.B.; Lee, H.G. Transient characteristics of a GdBCO racetrack pancake coil without turn-to-turn insulation. *Supercond. Sci. Technol.* **2014**, *27*, 015001. [[CrossRef](#)]
20. Hahn, H.; Park, D.K.; Bascunan, J.; Iwasa, Y. HTS pancake coils without turn-turn insulation. *IEEE Trans. Appl. Supercond.* **2011**, *21*, 1592–1595. [[CrossRef](#)]
21. Choi, S.; Jo, H.C.; Hwang, Y.J.; Hahn, S.; Ko, T.K. A Study on the no insulation winding method of the HTS coil. *IEEE Trans. Appl. Supercond.* **2012**, *22*, 4904004. [[CrossRef](#)]
22. Wang, Y.; Chan, W.K.; Schwartz, J. Self-protection mechanisms in no-insulation (RE)Ba<sub>2</sub>Cu<sub>3</sub>O<sub>x</sub> high temperature superconductor pancake coils. *Supercond. Sci. Technol.* **2017**, *29*, 045007. [[CrossRef](#)]
23. Zhang, Z.; Kim, C.H.; Kim, J.G.; Kvitkovic, J.; Pamidi, S.; Zhang, M.; Li, J.; Yuan, W. An Experimental Investigation of the Transient Response of HTS Non-insulation Coil. *J. Supercond. Nov. Magn.* **2017**, *30*, 387–393. [[CrossRef](#)]
24. Choi, Y.H.; Song, J.B.; Yang, D.G.; Kim, Y.G.; Lee, H.G. A novel no-insulation winding technique of high temperature-superconducting racetrack coil for rotating applications: A progress report in Korea university. *Rev. Sci. Instrum.* **2016**, *87*, 104704. [[CrossRef](#)] [[PubMed](#)]
25. Wang, Y.; Xu, D.; Li, Z.Y.; Jin, Z.; Hong, Z.; Song, H. An equivalent circuit grid model for no-insulation HTS pancake coils. *Supercond. Sci. Technol.* **2015**, *28*, 045017. [[CrossRef](#)]
26. Quides, M.R.; Sekino, M.; Ohsaki, H.; Kashima, N.; Nagaya, S. Electromagnetic Design Study of Transverse Flux Enhanced Type Superconducting Wind Turbine Generators. *IEEE Trans. Appl. Supercond.* **2011**, *21*, 1101–1104. [[CrossRef](#)]
27. Li, X.; Han, L.; Yang, X.; Zhang, D.; Zhang, J.; Xiao, L. Design and Model Test of the Racetrack Excitation Coil in a Novel High Temperature Superconducting Generator. *IEEE Trans. Appl. Supercond.* **2010**, *20*, 1081–1084.



28. Fukui, S.; Ogawa, J.; Sato, T.; Tsukamoto, O.; Kashima, N.; Nagaya, S. Study of 10 MW-Class Wind Turbine Synchronous Generators With HTS Field Windings. *IEEE Trans. Appl. Supercond.* **2011**, *21*, 1151–1154. [[CrossRef](#)]
29. Snitchler, G.; Gamble, B.; King, C.; Winn, P. 10 MW Class Superconductor Wind Turbine Generators. *IEEE Trans. Appl. Supercond.* **2011**, *21*, 1089–1092. [[CrossRef](#)]
30. Hwang, Y.J.; Choi, S.; Jang, J.Y.; Lee, J.; Yoon, Y.S.; Kim, H.M.; Chung, Y.D.; Jo, Y.-S.; Jang, M.H.; Al-Ammar, E.A.; et al. A Study on the Superconducting Synchronous Generator with the Fixed-Type Field Coil. *IEEE Trans. Appl. Supercond.* **2013**, *23*, 5200305. [[CrossRef](#)]
31. Jeong, J.-S.; An, D.-K.; Hong, J.-P.; Kim, H.J.; Jo, Y.-S. Design of a 10-MW-Class HTS Homopolar Generator for Wind Turbines. *IEEE Trans. Appl. Supercond.* **2017**, *27*, 5202804. [[CrossRef](#)]
32. Kim, J.M.; Jang, J.Y.; Lee, S.-G.; Hwang, Y.J. Characteristic Analysis of a HTS Flux-Switching Synchronous Generator with NI-Type HTS Field Coils. *IEEE Trans. Appl. Supercond.* **2018**, *28*, 5202705. [[CrossRef](#)]
33. Hwang, Y.J.; Ahn, M.C.; Lee, J.; Yoon, Y.S.; Kim, H.M.; Chung, Y.D.; Jo, Y.-S.; Kim, T.J.; Ko, T.K. Electromagnetic Design of a 15 MW-class HTS Flux Switching Synchronous Generator considering Mechanical Stress of the Rotor Core. *IEEE Trans. Appl. Supercond.* **2014**, *24*, 5202305.
34. Wang, Y.; Wang, C.; Feng, Q.; Li, X.; Ching, T.W. Design and Experiment of an HTS Flux-Switching Machine with Stationary Seal. *IEEE Trans. Appl. Supercond.* **2017**, *27*, 5201405. [[CrossRef](#)]
35. Zhao, J.; Zheng, Y.; Zhu, C.; Liu, X.; Li, B. A Novel Modular-Stator Outer-Rotor Flux-Switching Permanent-Magnet Motor. *Energies* **2017**, *10*, 937. [[CrossRef](#)]
36. Ullah, N.; Basit, A.; Khan, F.; Ullah, W.; Shahzad, M.; Zahid, A. Enhancing Capabilities of Double Sided Linear Flux Switching Permanent Magnet Machines. *Energies* **2018**, *11*, 2781. [[CrossRef](#)]
37. Kwon, J.-W.; Lee, J.-H.; Zhao, W.; Kwon, B.-I. Flux-Switching Permanent Magnet Machine with Phase-Group Concentrated-Coil Windings and Cogging Torque Reduction Technique. *Energies* **2018**, *11*, 2758. [[CrossRef](#)]
38. Yao, Y.; Liu, C.; Lee, C.H.T. Quantitative Comparisons of Six-Phase Outer-Rotor Permanent-Magnet Brushless Machines for Electric Vehicles. *Energies* **2018**, *11*, 2141. [[CrossRef](#)]
39. Incropera, F.P. *Fundamentals of Heat and Mass Transfer*; John Wiley & Sons: New York, NY, USA, 1996.
40. Kim, M.S.; Choi, Y.S.; Kim, D.L. Variable Temperature Cryostat for Cryogenic Temperature Sensor Calibration. *Supercond. Cryog.* **2012**, *14*, 46–49. [[CrossRef](#)]
41. Kim, J.M.; Jang, J.Y.; Chung, J.; Hwang, Y.J. A New Outer-Rotor Hybrid Excited Flux-Switching Machine Employing the HTS Homopolar Topology. *Energies* **2019**, *12*, 2654. [[CrossRef](#)]
42. Kim, K.L.; Choi, Y.H.; Yang, D.G.; Kang, D.H.; Kim, J.-H.; Kim, H.-M.; Lee, H.-G. Analytical and empirical studies on the characteristic resistances of no-insulation GdBCO racetrack pancake coil under various operating currents. *Curr. Appl. Phys.* **2015**, *15*, 8–13. [[CrossRef](#)]
43. Zhang, G.; Hua, W.; Cheng, M.; Zhang, J.; Jinag, W. Investigation of an Improved Hybrid-Excitation Flux-Switching Brushless Machine for HEV/EV Applications. *IEEE Trans. Ind. Appl.* **2015**, *51*, 3791–3799. [[CrossRef](#)]

